J. Fluid Mech. (1996), *vol.* 312, *pp.* 173–200

Stability of two-layer stratified flow in inclined channels: applications to air entrainment in coating systems

By YUAN C. SEVERTSON AND CYRUS K. AIDUN†

Institute of Paper Science and Technology and The George W. Woodruff School of Mechanical Engineering, Georgia Institute of Technology, 500 10th Street, N.W. Atlanta, GA 30318-5794, USA

(Received 11 November 1994 and in revised form 17 October 1995)

To understand the physics of air entrainment in thin-film liquid coating and other applications, the stability characteristics of general stratified two-layer Poiseuille–Couette flow are examined in inclined channels. Only one mode of instability, the interfacial mode, is obtained in the long-wave asymptotic limit. The generalized eigenvalue problem, formed by spectral decomposition and solution of the general two-layer Orr–Sommerfeld equation, is solved to obtain all of the critical modes. Analysis of the air/liquid interface corresponding to experiments reveals that because of the large density variation between the two layers, the interfacial mode is the only mode of instability in air entrainment. Results from the stability analysis of the flow near the contact line where air entrainment occurs are consistent with previous experimental observations.

1. Introduction

Stability of stratified fluid layers in inclined channels is important in many physical problems. Examples vary from flooding problems in channels to multilayer extrusion and coating flows. In this paper, however, we focus on the two-layer flow instability in inclined channels with applications to air entrainment in coating where the two fluids are air and the coating liquid.

A liquid coating process, where a thin liquid film is applied on a substrate, involves displacement of air by liquid. With flexible substrates, such as paper, photographic films, or magnetic tapes, the coating is continuously applied onto a moving surface. The wetting line where the liquid comes into contact with the dry substrate is referred to as the dynamic contact line. The speed of the substrate and, therefore, the rate of coating is limited by the maximum critical speed of displacing the air at the contact line. It was first noted by Deryagin & Levi (1959) that beyond a critical speed, the contact line which is originally straight breaks into a sawtooth pattern where a thin air layer penetrates between the liquid and the solid surface. This leads to the formation of air bubbles which penetrate into the liquid phase.

We recognize at least two regimes of air entrainment: (i) a microscopic regime, proposed by Miyamoto & Scriven (1982) and further investigated by Miyamoto (1991) and (ii) a second regime at macroscopic scale where air bubbles of the order of few hundred microns form at the wetting line and penetrate into the liquid.

† Author to whom correspondence should be sent.

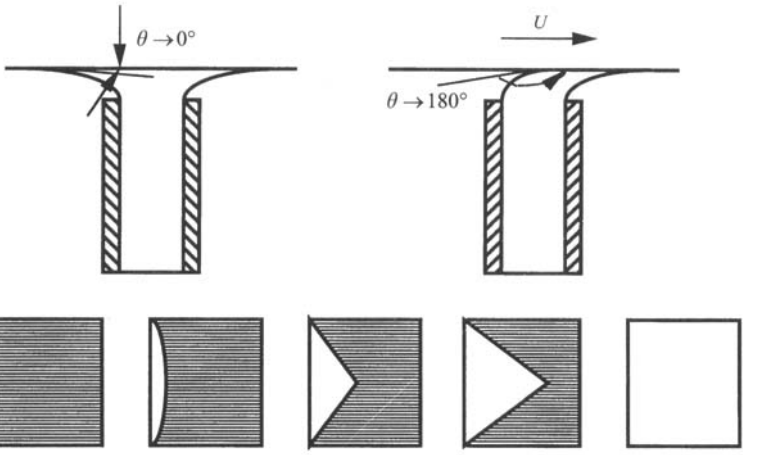

FIGURE 1. Schematic of the boundary displacement during wetting (from Deryagin & Levi 1959).

Our study focuses on the macroscopic regime of air entrainment where the entrained bubbles are too large to dissolve in the liquid and, therefore, remain in the system. We are primarily interested in the mechanism of the dynamic contact line instability and air entrainment with non-porous smooth surfaces although the general conclusions may apply to paper and photographic films, as well.

The pioneering work of Deryagin & Levi (1959) revealed an important event and limitation in the wetting of solids by liquid. A contact line, originally straight, breaks into a sawtooth pattern (figure 1) at a critical speed where the contact angle approaches 180°. This flow behaviour at the wetting line seems to be universal in the sense that it occurs regardless of the substrate material and liquid properties. In the ideal situation where the contact line is infinitely long, this behaviour can be viewed as a transition from a two-dimensional flow to a three-dimensional state.

Blake & Ruschak (1979) attributed this behaviour to a maximum wetting speed above which the contact line has to incline with the flow direction in order to experience a wetting speed below the maximum value. A rigorous analysis of the contact line instability and formation of triangular air pockets remains to be undertaken.

In a recent study, we (Aidun, Veverka & Scriven 1991) have investigated the sequence of events which lead to the formation of air bubbles and their entrainment into the liquid. Clearly, a prerequisite for air entrainment in the wetting process is the formation of these triangular structures. The events that follow this transition and lead to entrainment of air bubbles are revealed by Veverka & Aidun (1991) and Aidun, Veverka & Scriven (1992). In these studies, the experimental setup (figure 2) consists of a roll immersed halfway into a pool of liquid. The roll rotates with a constant speed forming a contact line as the surface enters the liquid. The fluid that adheres to the roll at the region emerging from the liquid is scraped off.

The triangular air pockets are clearly visible at the contact line, as shown in the first frame of figure 3. Considering this image to be at time zero, the next 11 frames demonstrate the sequence of events leading to an air bubble entraining into the liquid phase. The markers on the horizontal lines on the roll are 1 cm apart. The reflection of the markers is also apparent in frames 43 to 58. The thinner cross-hairs on the camera lens divide the images into six parts. The three vertical lines are 16.3 mm apart. In these images, the solid surface is moving upward at a linear speed of $0.26\,\mathrm{m\,s^{-1}}$.

The solid surface inside the air pockets represented by the darker triangles is dry

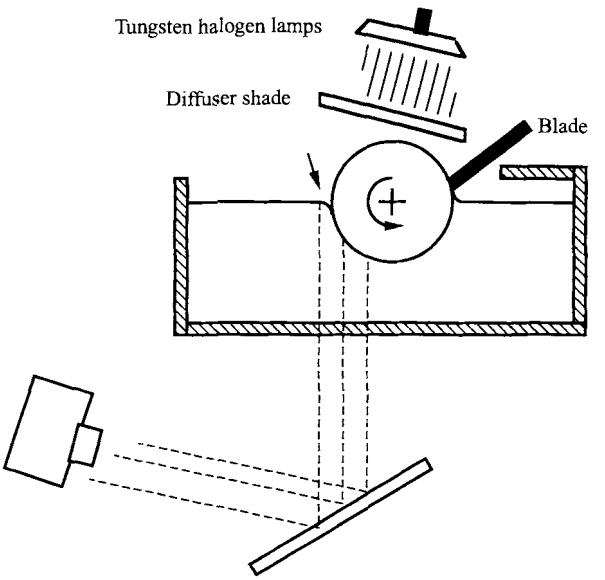

FIGURE 2. Schematic of the experimental setup.

and, therefore, the wetting line has a sawtooth structure. We explain the events leading to air entrainment by focusing on the second triangle from the left-hand side of frames 43 to 58 of figure 3. In general, the liquid ruptures the air film at the sides of the triangle creating a nucleation of wetting site which expands rapidly isolating an air patch at the tip as shown in frames 43 to 54. This volume of air detaches from the surface (frame 55) and forms an air bubble which penetrates into the liquid phase as demonstrated in frames 56 and 58. The total elapsed time from nucleation of wetting to formation of an air bubble is about 0.05 s. By measuring the volume of the bubble and the surface area of the triangle, we estimate the thickness of the air film to be between 10 to 50 μm. This is in good agreement with the value proposed by Scriven (1982).

Although the formation of air bubbles has been revealed by these images, the physical mechanism initiating air film rupture and the nucleation of wetting remains hidden with this particular flow visualization technique. In principle, there are two completely different mechanisms which can initiate a liquid bridge. A hydrodynamic mechanism involving wave formation on the liquid surface inside the air pocket is proposed by Scriven (1982). The wave amplitude could grow large enough to eventually touch the solid surface. The second mechanism could be due to particles in the fluid or air which penetrate into the air pocket and provide a bridge between the solid and the liquid. Obviously, in the presence of particles in the air, the second mechanism can initiate nucleation of wetting. The question, however, is whether the hydrodynamic mechanism is sufficient for initiating a wetting site. In other words, is the liquid surface inside the air pocket unstable and if so, what is the mechanism of this instability?

Experiments where the air pockets are viewed in a different angle show that waves form at the liquid surface. In this setup, we focus on the liquid interface inside the air pockets. The first picture in figure 4 shows a wavy surface at the two sides of the triangle. The subsequent pictures show wetting sites initiating at the sides followed by the same sequence of events leading to formation and entrainment of air bubbles, as

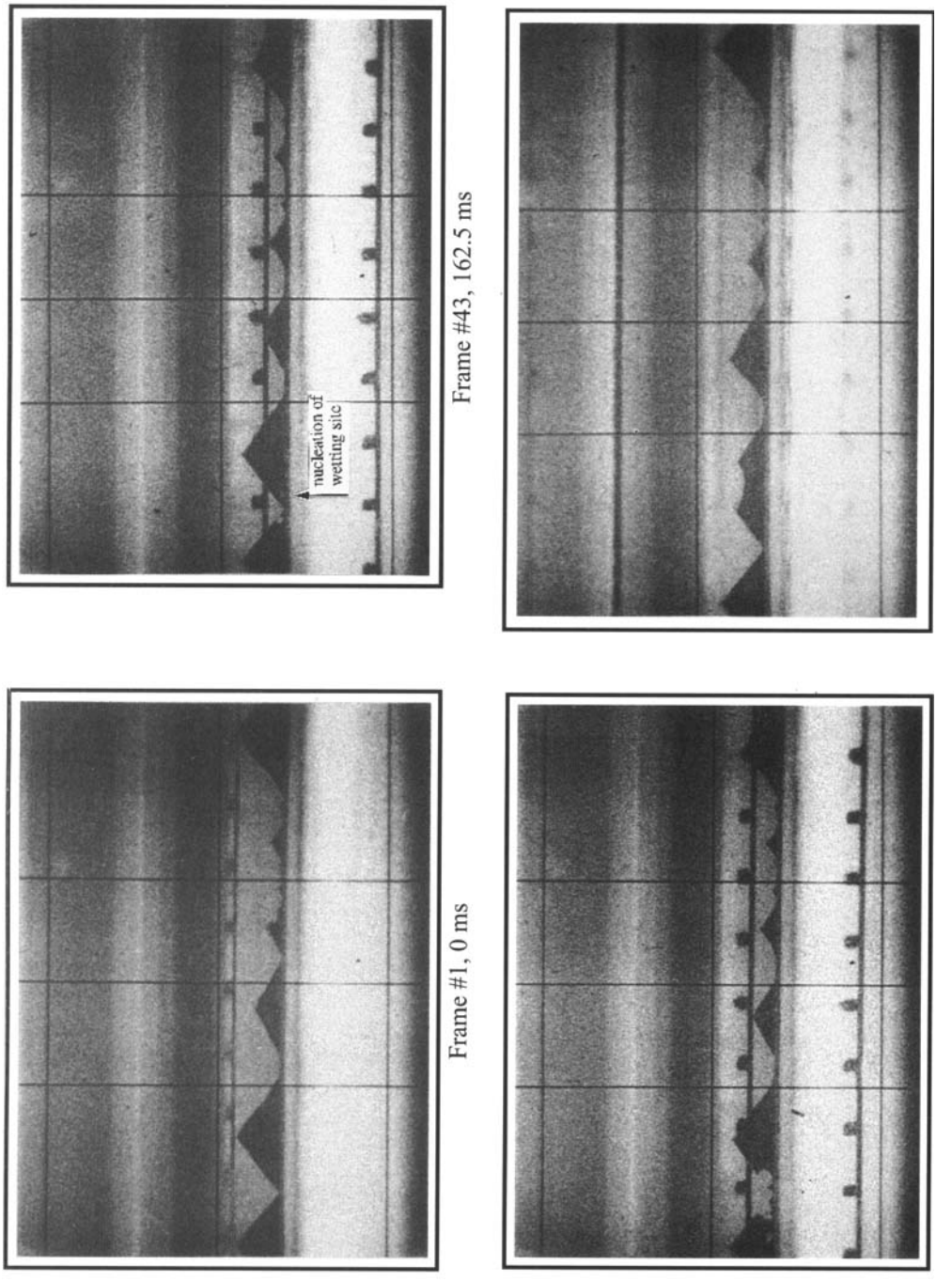

FIGURE 3. For caption see p. 179.

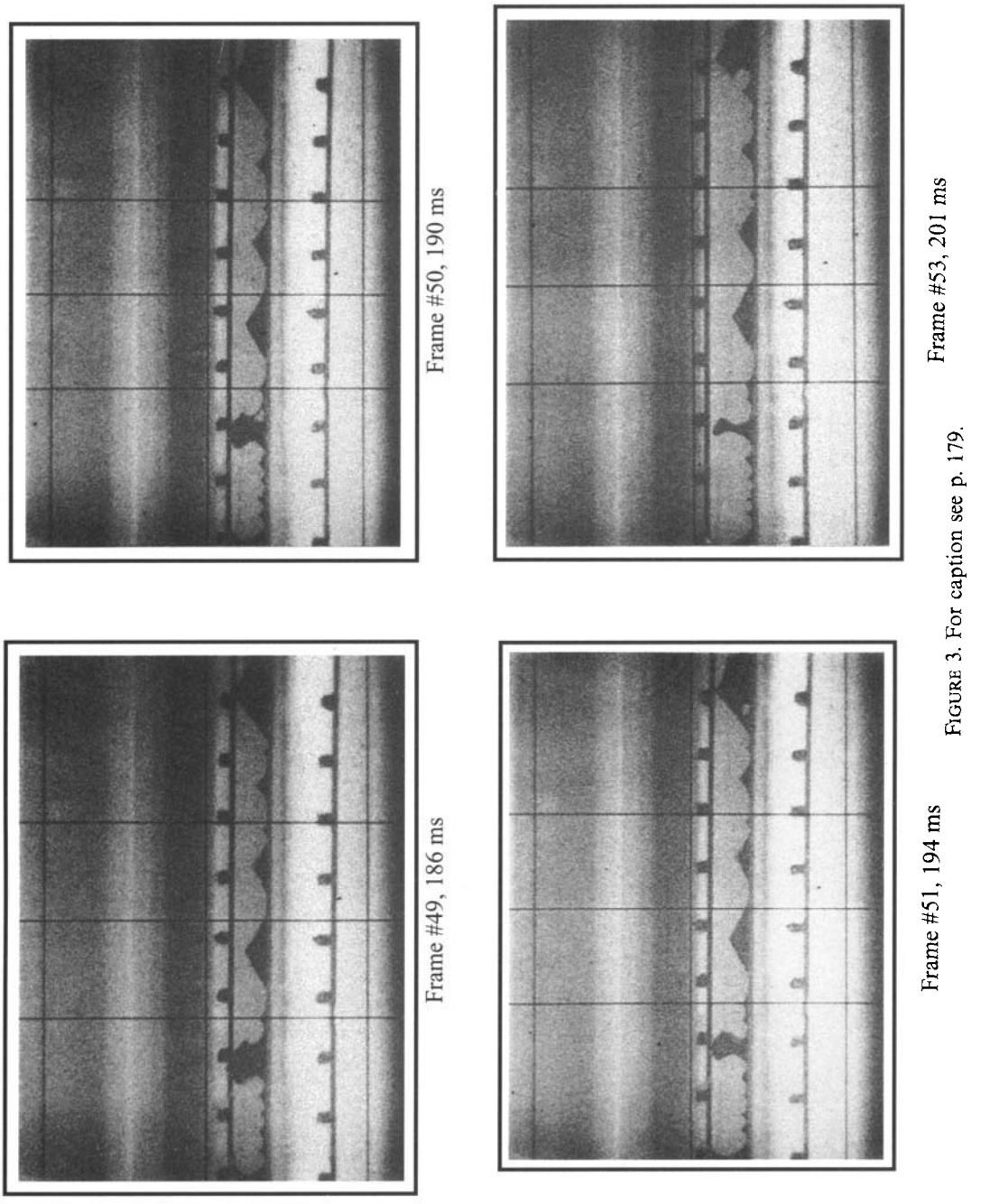

FIGURE 3. For caption see p. 179.

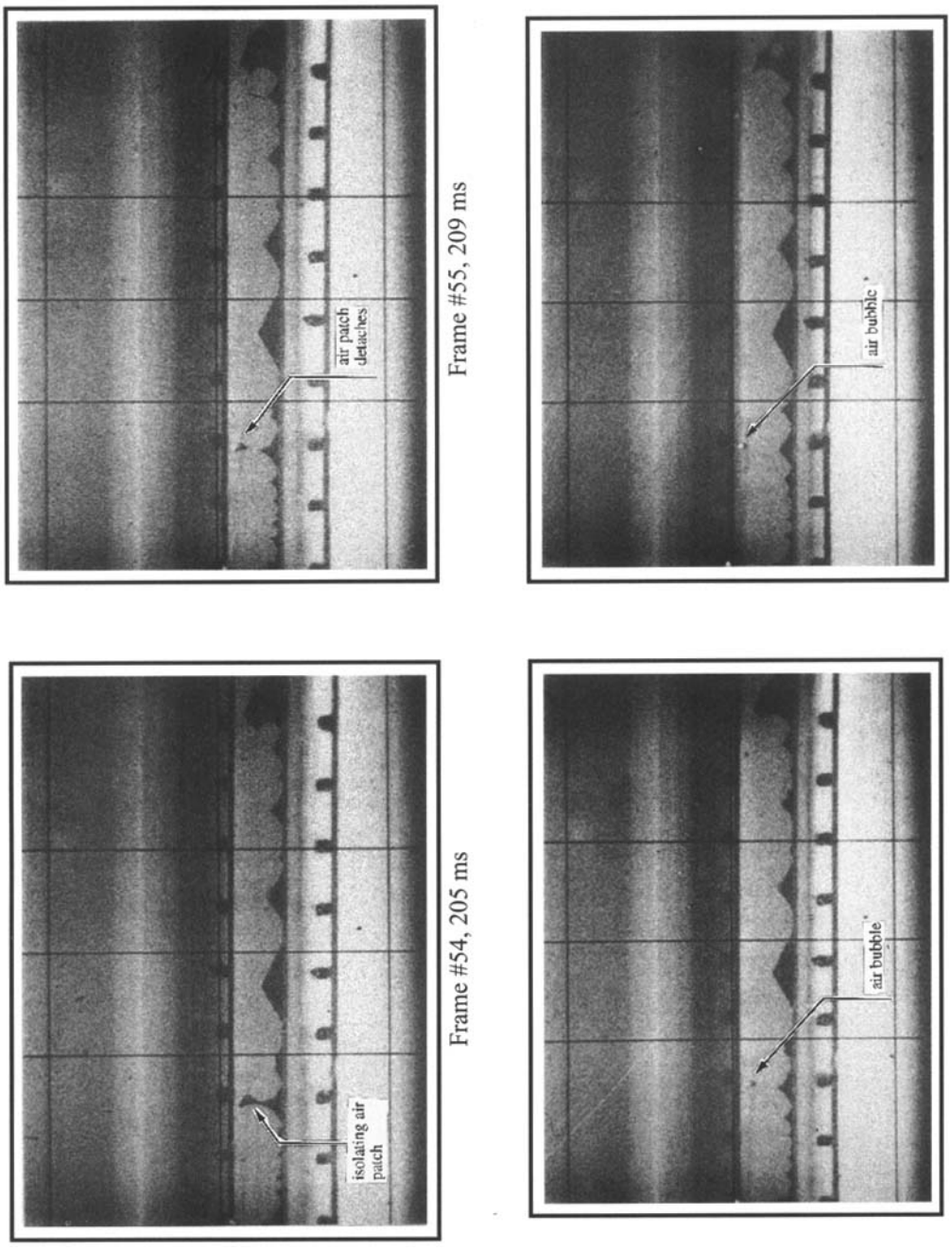

FIGURE 3. For caption see facing page.

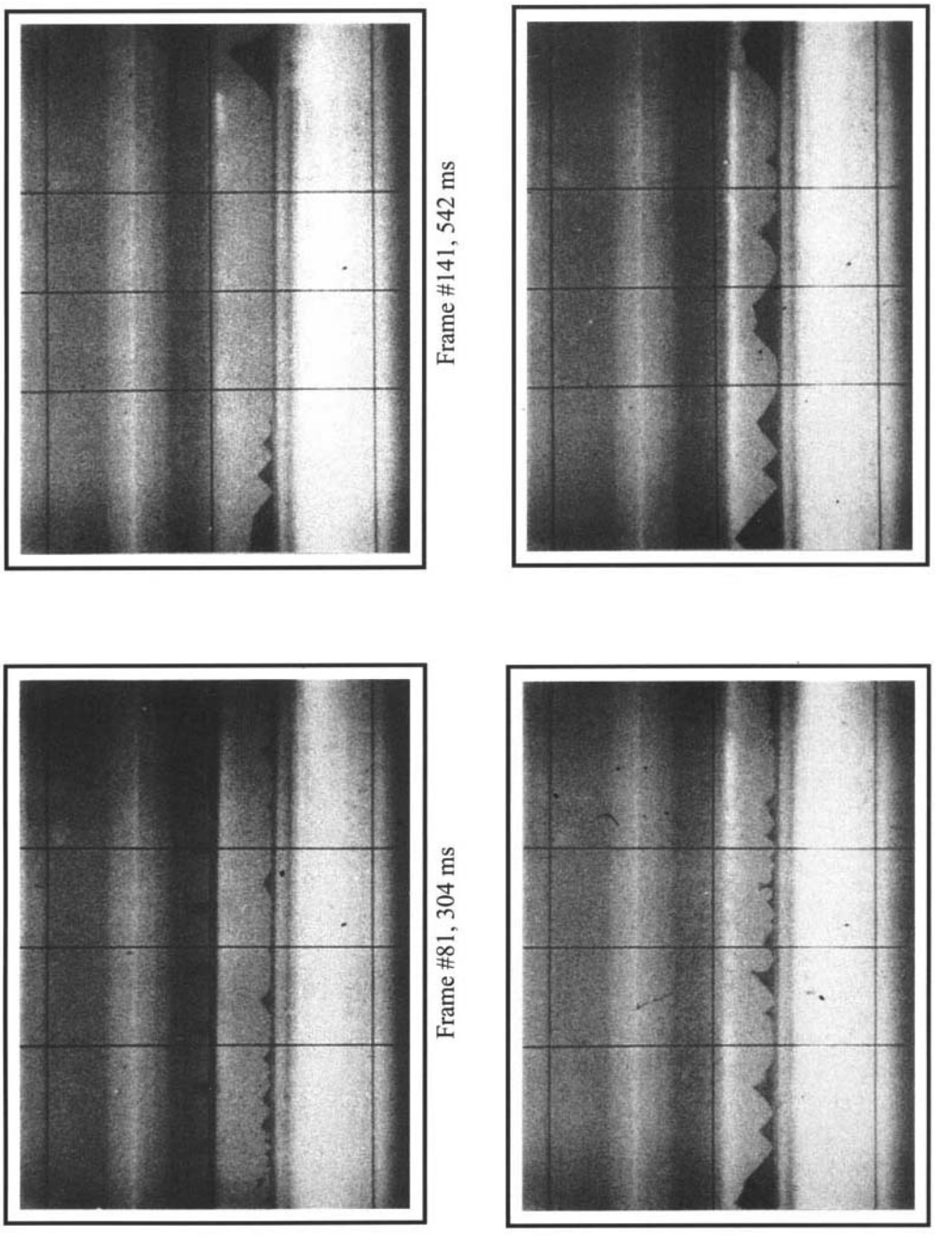

FIGURE 3. A selection from frames 1 to 241 of the 16 mm film showing the dynamics of air entrainment. The elapsed time is shown under each picture.

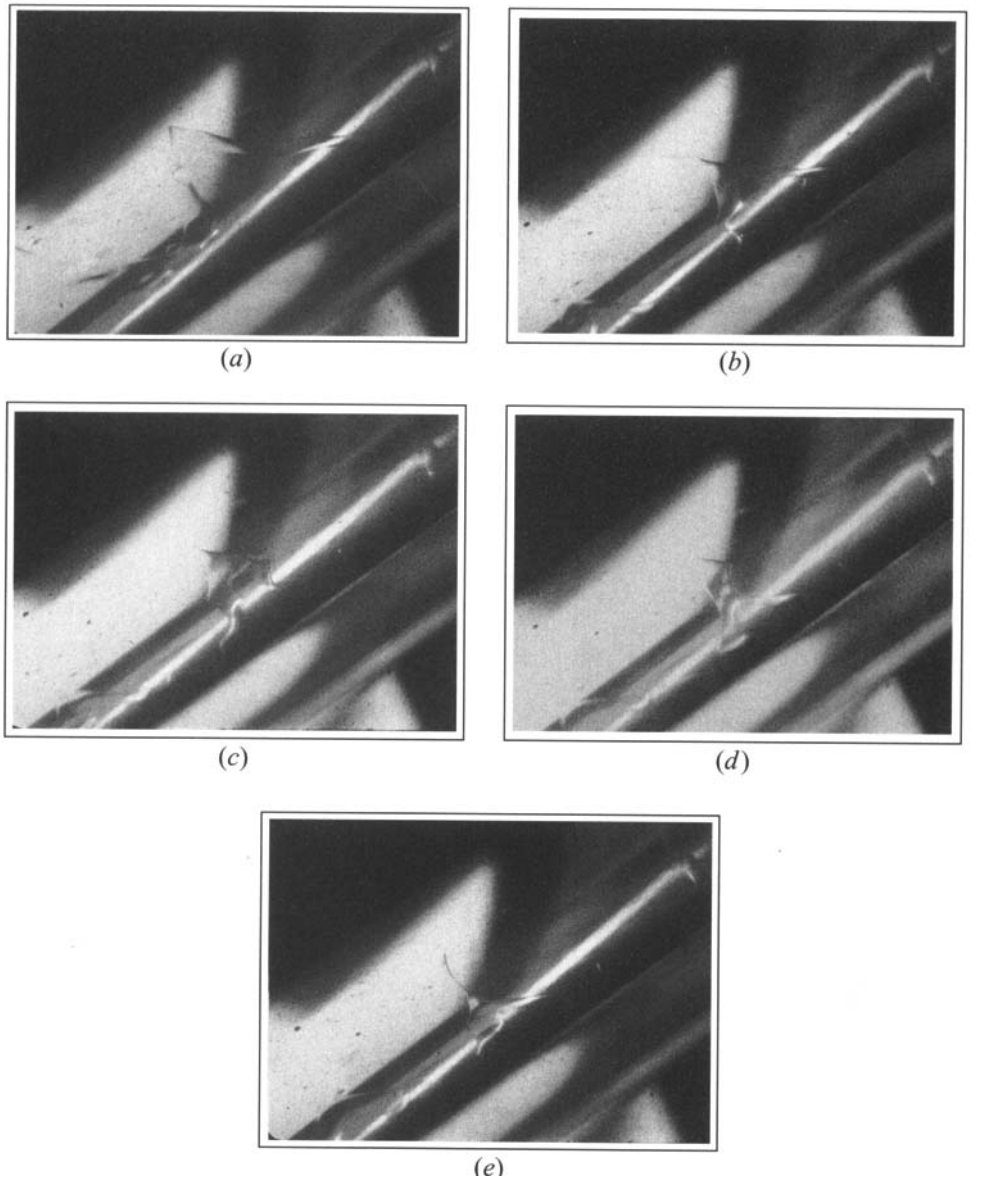

FIGURE 4. Sequence of events reproduced from the 16 mm film of the wavy interface inside the triangular air pockets at: (*a*) $t = 0$ ms, (*b*) $t = 25$ ms, (*c*) 59 ms, (*d*) 93ms, and (*e*) 506 ms.

presented above. The waves appear to travel toward the base of the triangle opposite to the direction of the solid surface motion. This is due to the air movement inside the air pocket. Air moves inward at the mid-part of the triangle, as shown in figure 5(*a*), and leaves the air pocket from the sides. These waves have a wavelength in the order of few mm, while their amplitude is orders of magnitude smaller.

The motivation for this study is to examine the stability characteristics of the air/liquid system inside the air pockets and to examine the mechanism(s) for potential instabilities.

The flow visualization results suggest that air flows into the air pocket with the solid surface at the mid-part of the triangle base, changes direction, and moves

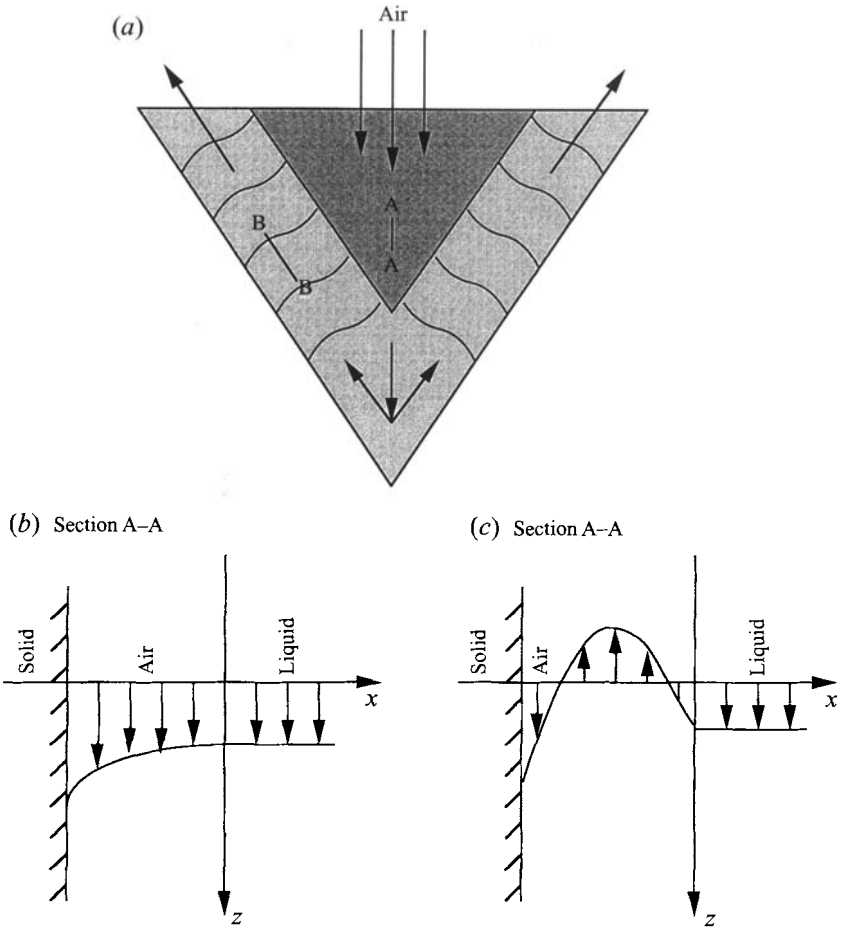

FIGURE 5. Schematics of (*a*) the triangular air layer, and the idealized air stream velocity profile in (*b*) cross-section A-A and (*c*) cross-section B-B.

outward along the sides. This clearly results in a complex three-dimensional flow pattern. For a rigorous stability analysis, one must solve the three-dimensional base state and examine its stability to spatial as well as temporal disturbances. A full stability analysis, however, is beyond the scope of this study and shall be addressed in the future. In this study, we note that the thickness of the air layer is orders of magnitude smaller than the other two dimensions. Taking advantage of this fact and assuming that lubrication approximations apply, we unfold the problem into its two-dimensional idealization, presented in figure 5, where schematics of the velocity profiles at sections A-A and B-B of figure 5(*a*) are plotted in figures 5(*b*) and 5(*c*), respectively. We have reduced the problem to the stability analysis of a stratified parallel flow in an inclined channel. Although multilayer stratified flows have been studied extensively in the past, the stability analysis of stratified Couette–Poiseuille flow in inclined channels applying to our problem has not been reported before.

The idealized system can be considered as the stratified Poiseuille–Couette flow of two immiscible liquids with different density and viscosity bounded by two parallel walls. One of the walls, representing the substrate, is moving while the other is stationary. Gravity is acting on the system at an angle varying from 0° to 90° relative

to the wall. Linear stability analysis of similar flow systems (two-layer parallel flows) has received much attention in recent years. In the following paragraphs, we briefly review the main points of these studies and list the unstable modes that have been observed in two-layer parallel flows. We then outline the unique features of the air entrainment problem which are not covered by previous studies.

It is well-known that one-layer parallel Poiseuille flow exhibits finite-amplitude subcritical instability (Reynolds & Potter 1967) and that the effect of the Couette component on the stability of such a system is stabilizing. The combined Poiseuille–Couette flow becomes stable to infinitesimal disturbances after superposing enough Couette component at a given Reynolds number. Whether the Couette component has the same stabilizing effect on the two-layer flow has remained unexplored.

Using a long-wave asymptotic method, Yih (1967) showed that in the presence of a viscosity difference between two fluids, plane Poiseuille and plane Couette flow can be unstable even at extremely small Reynolds numbers (Re). This unstable mode is in the neighbourhood of a hidden neutral mode for the single-layer case and is brought out by the viscosity stratification. A characteristic of the interfacial mode is that the magnitudes of the critical parameters grow as k^2, where k is the wavenumber. In his study, the two fluids have the same density but different viscosities, gravity is acting in the direction normal to the flow direction, and only stability in the long-wave region was investigated.

Linear stability analysis of the two-layer concurrent Couette flow of different viscosities in an infinite region indicates that in the absence of surface tension the flow is always unstable (Hooper & Boyd 1983). Hooper & Boyd (1987) showed that the relevant dimensionless groups in a two-layer Couette flow with the lower fluid bounded by the wall are a dimensionless wavenumber measured on a viscous lengthscale, β, and $(\alpha R)^{1/3}$, where α is a dimensionless wavenumber measured on the scale of the depth of the lower fluid, and R is the Reynolds number of the lower fluid. Three different kinds of unstable modes were found in different parameter regions. They concluded that there is a short-wave instability when β is large and at small β and $(\alpha R)^{1/3}$, a long-wave mode similar to Yih's appears. At small β, but large $(\alpha R)^{1/3}$, the dynamics are dominated by a new type of large Reynolds number instability which is due to the effect of the viscous boundary layer at the wall on the inviscid flow that could exist on either side of the interface.

After redefining α as a measure of the fluid shear rate, Hooper (1989) applied the above theory to the Couette–Poiseuille flows of two fluids of different viscosities but equal density confined in a two-dimensional channel. She noted that when $\beta \gg 1$ or $\beta \ll 1$ and $(\alpha R)^{1/3} \ll 1$ the stability of the flow is dominated by viscous effects at the interface, and the instability is caused primarily by a transfer of energy from the basic flow to the disturbance by the disturbance tangential stress at the interface. On the other hand, when $\beta \ll 1$ and $(\alpha R)^{1/3} \gg 1$, the instability of the flow is dominated by viscous effects at the boundary walls caused mainly by a transfer of energy from the basic flow to the disturbance via the Reynolds stress.

The thin-layer effect is referred to the following phenomenon in the two-layer Couette flow with gravity normal to the flow direction. If the two layers have the same density, the unstable long-wave mode can be stabilized if the less-viscous fluid is the thinner layer. Even in the case of two layers with an adverse density stratification, the critical long-wave mode can be stabilized by placing the less-viscous fluid in the thinner layer (Renardy 1987). The interfacial mode is always stable in the short-wave region due to the surface tension effects.

The combined effects of density, viscosity stratification and thickness ratio as well as

the effects of interfacial tension and gravity on the parallel plane Poiseuille flow have been investigated by Yiantsios & Higgins (1988). They showed that the interfacial mode is unstable for a large range of the physical parameters, while the shear mode is unstable in a much smaller region. Also the maximum growth rate for the interfacial mode is about two orders of magnitude larger than that for the shear mode, even when the Reynolds number for the interfacial mode is smaller. Although the case studied by Yiantsios & Higgins (1988) has similar features to our problem, there are two major differences. First, in their study, gravity acts normal to the flow direction, and therefore has no effect on the base flow. Gravity enters the calculations only in the disturbed normal stress boundary condition. However, with the presence of the inclined walls in our problem, gravity not only plays an important role in the base flow, but also appears in both disturbed normal stress and tangential stress boundary conditions. Secondly, they only consider pure Poiseuille flow whereas in our problem the Couette component has a significant effect on the results, an effect that needs to be studied.

Air entrainment can also occur when a jet of liquid plunges into a stagnant pool of the same liquid. This problem was studied by Lezzi & Prosperetti (1991) who represented the problem as a parallel liquid/air/liquid flow problem. In their study, they assumed that the liquid layer has no velocity gradient and, therefore, simplified the problem by imposing a constant velocity at each air/liquid interface. In addition to the interfacial instability due to the viscosity stratification, critical Kelvin–Helmholtz modes appear in the system. In the current problem, where one side of the air layer is bounded by a solid surface, we show that the Kelvin–Holmholtz modes of instability are totally excluded.

One-layer thin liquid systems down an inclined wall can be classified into two groups. In the first group, a fixed stress is imposed on the top surface, while the second group is characterized by an imposed velocity (Smith 1990). The physical mechanism for the long-wave instability can be decomposed into an initiating mechanism that drives the dominant motion in the film and a growth mechanism that produces the unstable mode at the interface. The initiating mechanism can be either velocity-induced or stress-induced. Smith (1990) predicted that in flows composed of more than one liquid layer, both mechanisms can be important. When each layer has a different density, a jump in the curvature of the base velocity profile at the interface would occur, and the stress-initiation mechanism would dominate. Likewise, when viscosity stratification is presented, a jump in the base velocity gradient across the interface would appear, and the velocity-initiation mechanism would operate.

Using a zero Reynolds number approximation, Loewenherz & Lawrence (1989) showed that for two-layer parallel flows down an inclined wall with a free surface both long-wave and finite-wave modes are unstable. In their paper, surface tension was neglected, and the density was the same for both layers.

Recently, Tilley, Davis & Bankoff (1994) studied the stability of two-layer Poiseuille flow in an inclined channel. They found that the primary instability in the cases they considered is due to long-wave interfacial disturbances. They have also reported that the odd Orr–Sommerfeld shear mode could become unstable and even dominant in some parameter region. The focus of their study was the flooding problem in inclined channels and their analysis in arbitrary wave regions concentrated on air–water and olive oil–water systems. On the other hand, we are interested in understanding the mechanism(s) causing air entrainment in coating systems where one of the surface is moving and the coating viscosity is orders of magnitude larger than water. We consider the base flow patterns that are visualized in our previous air entrainment

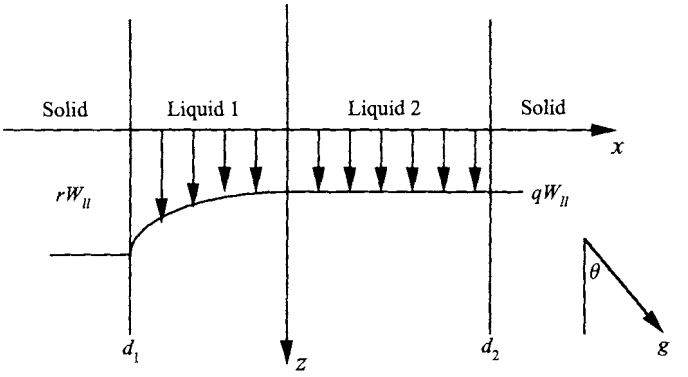

FIGURE 6. Flow configuration.

experiments in order to understand the physical mechanism(s) of the instability in the experiments. We have not encounter the odd Orr–Sommerfeld shear mode revealed by Tilley *et al.* (1994) in the air entrainment problem considered here.

Although a lot of research has been done on two-layer parallel flows, none has considered the stability characteristics of general two-layer flow with surface tension in an inclined Couette–Poiseuille system with density and viscosity stratification. To better understand the physics of air entrainment in coating and other surface processing applications, it is necessary to make a generalized model which can be used to explain the experimental observations and, in particular, to determine whether the waves observed at the air/liquid interface are due to hydrodynamic effects alone or influenced by other physical effects.

2. Governing equations

The goal of this section is the development of generalized linear stability equations for two-layer parallel flow systems (figure 6). The problem is defined as two immiscible liquids confined between two solid walls. The left wall is moving at a velocity of rW_{II}, and the right at a velocity of qW_{II}, where q and r serve as parameters. Indices 1 and 2 are used to denote layers 1 and 2, respectively. The coordinate system is introduced with the z-axis parallel to the walls and x in the direction normal to the walls. Gravity is acting on the system with an angle θ to the z-direction, as shown in figure 6.

The equations are non-dimensionalized with respect to the thickness of layer 1, d_1, for length, W_{II} for velocity, $\mu_1 W_{II}/d_1$ for pressure, and $\rho_1 d_1^2/\mu_1$ for time. This introduces the dimensionless parameters

$$\text{viscosity ratio} \quad m = \frac{\mu_1}{\mu_2}, \tag{1}$$

$$\text{density ratio} \quad e = \frac{\rho_1}{\rho_2}, \tag{2}$$

$$\text{thickness ratio} \quad n = \frac{d_2}{d_1}, \tag{3}$$

$$\text{Reynolds number} \quad Re = \frac{\rho_1 d_1 W_{II}}{\mu_1}, \tag{4}$$

$$\text{Froude number} \quad F = \frac{\rho_1 g d_1^2 (1 - 1/e)}{\mu_1 W_{II}}, \tag{5}$$

$$A_1 = \frac{\left(\mathrm{d}p/\mathrm{d}z - \rho_1 g \cos(\theta)\right) d_1^2}{2\mu_1 W_{II}}, \tag{6}$$

$$A_2 = \frac{\left(\mathrm{d}p/\mathrm{d}z - \rho_2 g \cos(\theta)\right) d_1^2}{2\mu_1 W_{II}}, \tag{7}$$

where $\mathrm{d}p/\mathrm{d}z$ is the pressure gradient in the z-direction, and g is the gravitational acceleration. The Reynolds number, Re, is defined in terms of the parameters of layer 1 and W_{II}, as shown in (4). The flow may be generated by pressure gradient, gravity, or the movement of the walls, or their combination. Therefore, in some cases not only the Reynolds number but also the Froude number, F, defined by (5) are the important parameters.

In this analysis, we assume the base flow is fully developed steady laminar flow. The base velocities can be expressed as

$$W_1 = A_1 x^2 + a_1 x + b_1, \tag{8}$$

$$W_2 = m A_2 x^2 + a_2 x + b_2, \tag{9}$$

subject to the following boundary conditions:

$$W_1(-1) = r, \qquad W_2(n) = q, \tag{10}$$

$$W_1(0) = W_2(0), \qquad m\frac{\mathrm{d}W_1}{\mathrm{d}x}(0) = \frac{\mathrm{d}W_2}{\mathrm{d}x}(0). \tag{11}$$

The coefficients in the base velocity profile are

$$a_1 = \frac{A_1 - A_2 m n^2 - r + q}{1 + mn}, \qquad a_2 = m\, a_1, \tag{12}$$

$$b_1 = \frac{-(A_1 + A_2 n) mn + mnr + q}{1 + mn}, \qquad b_2 = b_1. \tag{13}$$

The system is perturbed by imposed infinitesimal velocity ($\boldsymbol{u}_i = (u_i, \omega_i)$) and pressure ($p_i$) disturbances on layer i, in addition to a position disturbance (η) on the interface. Neglecting the quadratic and higher-order terms, we obtain the linearized disturbance equations. Among these, the continuity equation allows the use of the stream function ψ_i for each layer such that

$$u_i = -\frac{\partial \psi_i}{\partial z}, \quad \omega_i = \frac{\partial \psi_i}{\partial x}. \tag{14}$$

In the linear stability analysis, we assume that the solution to the disturbed system is periodic in the z-direction with wavenumber k. Thus, all the disturbances can be expressed in normal modes as

$$\begin{pmatrix} \psi_i(x,z,t) \\ p_i(x,z,t) \\ \eta(z,t) \end{pmatrix} = \begin{pmatrix} \hat{\psi}_i(x) \\ \hat{p}_i(x) \\ \hat{\eta} \end{pmatrix} \mathrm{e}^{st + \mathrm{i}kz}, \tag{15}$$

where s, the growth rate, with positive (negative) real part represents instability (stability). The resulting equation is the well-known Orr–Sommerfeld equation, given by

$$\hat{\psi}_i^{\mathrm{iv}} - 2k^2 \hat{\psi}_i'' + k^4 \hat{\psi}_i = \frac{\xi_i}{\varsigma_i} \left[(s + \mathrm{i}kReW_i)(\hat{\psi}_i'' - k^2 \hat{\psi}_i) - \mathrm{i}kReW_i'' \hat{\psi}_i \right], \tag{16}$$

where

$$\xi_i = \begin{cases} 1, & i=1 \\ e, & i=2 \end{cases}; \quad \varsigma_i = \begin{cases} 1, & i=1 \\ 1/m, & i=2 \end{cases}, \tag{17}$$

subject to the no-slip conditions at the walls

$$\hat{\psi}_1(-1) = 0, \quad \hat{\psi}_1'(-1) = 0, \tag{18}$$

$$\hat{\psi}_2(n) = 0, \quad \hat{\psi}_2'(n) = 0. \tag{19}$$

The continuity of each component of velocity at the interface is given by

$$\hat{\psi}_1(0) = \hat{\psi}_2(0), \tag{20}$$

$$\hat{\psi}_1'(0) - \hat{\psi}_2'(0) = \left[W_2'(0) - W_1'(0)\right]\hat{\eta}, \tag{21}$$

while the continuity of tangential and normal stresses yields

$$m\left[\hat{\psi}_1''(0) + k^2\hat{\psi}_1(0)\right] = \hat{\psi}_2''(0) + k^2\hat{\psi}_2(0) + \left[W_2''(0) - mW_1''(0)\right]\hat{\eta}, \tag{22}$$

$$\left[\hat{\psi}_1'(0)s^* - ikRe\hat{\psi}_1(0)W_1'(0)\right] - \frac{1}{e}\left[\hat{\psi}_2'(0)s^* - ikRe\hat{\psi}_2(0)W_2'(0)\right]$$
$$- \left[\hat{\psi}_1'''(0) - 3k^2\hat{\psi}_1'(0)\right] + \frac{1}{m}\left[\hat{\psi}_2'''(0) - 3k^2\hat{\psi}_2'(0)\right] = \mathrm{i}\left[kF\sin(\theta) - (Ca)^{-1}k^3\right]\hat{\eta}, \tag{23}$$

where the capillary number, Ca, and s^* are defined by

$$Ca = \frac{\mu_1 W_{ll}}{\sigma}, \tag{24}$$

and

$$s^* = s + ikReW_1(0), \tag{25}$$

where σ is the surface tension.

The kinematic condition is presented by

$$s^*\hat{\eta} = -ikRe\hat{\psi}_1(0). \tag{26}$$

Equations (16)–(26) form an eigenvalue problem with the eigenvalue s and the eigenfunction given by $\hat{\psi}_i$ and η for a given set of parameters k, Re, m, e, n, Ca, and F. We first solve this problem in the asymptotic limit, $k \ll 1$, representing the long-wave instability of the two-layer parallel flow. A full solution of the problem is also presented below.

3. Long-wave asymptotic analysis

Before solving for the flow instability numerically, some important information can be obtained from its asymptotic behaviour in the long-wave limit, where $k \ll 1$.

3.1. *Viscous/inviscid analysis*

The experimental results have shown that the air layer is much thinner than the liquid. Thus, as the first step, we assume that the liquid extends to infinity with a constant velocity. In this way, the difference between the interface velocity and the free-stream liquid will be proportional to the viscosity ratio, m. Since in reality the ratio is much smaller than one, the shear stress at the air/liquid interface is neglected

here. Therefore, the velocity of the liquid layer is considered as uniform to simplify the calculation.

Considering air in layer 1 and liquid in layer 2, we approximate the velocity gradient in the liquid layer to be zero, $m = 0$. With this approximation together with the difference between the two velocity coefficients being unity, i.e. $r - q = 1$, the coefficients for the base-state solution (12) and (13) reduce to

$$a_1 = A_1 - 1, \qquad a_2 = 0, \tag{27}$$

$$b_1 = q, \qquad b_2 = q. \tag{28}$$

We define the reduced velocity W_i^* by subtracting the liquid velocity from the base flow, that is

$$W_i^* = W_i - W_2. \tag{29}$$

The linearized equations in the liquid phase are given by

$$\nabla \cdot \boldsymbol{u}_2 = 0 \tag{30}$$

$$\frac{\partial \boldsymbol{u}_2}{\partial t} = -e\nabla p_2, \tag{31}$$

while the equations for the air layer are

$$\nabla \cdot \boldsymbol{u}_1 = 0, \tag{32}$$

$$\frac{\partial u_1}{\partial t} + ReW_1^* \frac{\partial u_1}{\partial z} = -\frac{\partial p_1}{\partial x} + \nabla^2 u_1, \tag{33}$$

$$\frac{\partial \omega_1}{\partial t} + Re\left[W_1^* \frac{\partial \omega_1}{\partial z} + u_1 \frac{\mathrm{d}W_1^*}{\mathrm{d}x}\right] = -\frac{\partial p_1}{\partial z} + \nabla^2 \omega_1 . \tag{34}$$

The boundary conditions are simplified as no slip at the left wall

$$u_1(-1, z, t) = \omega_1(-1, z, t) = 0, \tag{35}$$

while the continuity equations of normal and tangential velocities at the interface are given respectively by

$$u_1(0, z, t) = u_2(0, z, t) \tag{36}$$

and

$$\omega_1(0, z, t) = \omega_2(0, z, t) - W_1'(0)\eta(z, t), \tag{37}$$

and the continuity of normal stress at the interface is given by

$$p_1(0, z, t) - p_2(0, z, t) = 2\left[\frac{\partial u}{\partial x}(0, z, t) - W_1'(0)\frac{\partial \eta}{\partial z}\right] - (Ca)^{-1}\frac{\partial^2 \eta}{\partial z^2}. \tag{38}$$

The kinematic condition reduces to

$$\frac{\partial \eta}{\partial t} = Re\ u_1(0, z, t). \tag{39}$$

By the usual procedure of using the normal modes,

$$\begin{pmatrix} u_i(x, z, t) \\ \omega_i(x, z, t) \\ p_i(x, z, t) \end{pmatrix} = \begin{pmatrix} \hat{u}_i(x) \\ \hat{\omega}_i(x) \\ \hat{p}_i(x) \end{pmatrix} \mathrm{e}^{st + \mathrm{i}kz}, \tag{40}$$

the solution to the liquid phase (30) and (31) can be written as

$$\hat{u}_2(x) = C_2 \mathrm{e}^{-kx}, \tag{41}$$

$$\hat{\omega}_2(x) = -\mathrm{i}C_2\mathrm{e}^{-kx}, \tag{42}$$

$$\hat{p}_2(x) = \frac{s}{ek}C_2\mathrm{e}^{-kx}, \tag{43}$$

where C_2 is the integration constant.

Other unknowns are expanded in terms of the wavenumber k in a similar form to that used by Lezzi & Prosperetti (1991),

$$\begin{pmatrix} \hat{\omega}_1(x,k) \\ \hat{\eta}(k) \end{pmatrix} = \begin{pmatrix} \omega_{10}(x) \\ \eta_0 \end{pmatrix} + k \begin{pmatrix} \omega_{11}(x) \\ \eta_1 \end{pmatrix} + \ldots, \tag{44}$$

$$\begin{pmatrix} \hat{u}_1(x,k) \\ \hat{p}_1(x,k) \\ s(k) \end{pmatrix} = k \begin{pmatrix} u_{10}(x) \\ p_{10}(x) \\ s_0 \end{pmatrix} + k^2 \begin{pmatrix} u_{11}(x) \\ p_{11}(x) \\ s_1 \end{pmatrix} + \ldots . \tag{45}$$

Substituting the above expansions into (32)–(34) and then balancing the zeroth-order terms in k, we get the zeroth-order disturbance equations

$$u'_{10}(x) = -\mathrm{i}\,\omega_{10}(x), \tag{46}$$

$$u''_{10}(x) = p'_{10}(x), \tag{47}$$

$$\omega''_{10}(x) = 0. \tag{48}$$

The corresponding zeroth-order boundary conditions from (35)–(39) are given by

$$u_{10}(-1) = 0, \tag{49}$$

$$\omega_{10}(-1) = 0, \tag{50}$$

$$ku_{10}(0) = \hat{u}_2(0), \tag{51}$$

$$\omega_{10}(0) = -W'_1(0)\eta_0, \tag{52}$$

$$p_{10}(0) = (s_0/e)\,u_{10}(0) + 2\,\left[u'_{10}(0) - \mathrm{i}\,W'_1(0)\eta_0\right], \tag{53}$$

$$Re\,u_{10}(0) = s_0\eta_0. \tag{54}$$

The zeroth-order solution to the (46)–(48) with boundary conditions (49)–(52) is in the form

$$u_{10}(x) = \tfrac{1}{2}\mathrm{i}W'_1(0)\,\eta_0\,(x+1)^2, \tag{55}$$

$$\omega_{10}(x) = -W'_1(0)\,\eta_0\,(x+1), \tag{56}$$

$$p_{10}(x) = \mathrm{i}W'_1(0)\,\eta_0\,(x+1) + C_1, \tag{57}$$

where C_1 is the integration constant. Substituting the above solution into (53) and (54), the zeroth-order growth rate can be expressed as

$$s_0 = \tfrac{1}{2}\mathrm{i}\,Re\,W'_1(0) \tag{58}$$

and

$$C_1 = \left(\frac{s_0}{e} - 2\right)u_{10}(0). \tag{59}$$

Since s_0 is purely imaginary, it does not give any information about the stability. Therefore, the first-order correction is needed. The first-order disturbance equations are

$$u'_{11}(x) = -\mathrm{i}\,\omega_{11}(x), \tag{60}$$

$$u''_{11}(x) = p'_{11}(x) + s_0\,u_{10} + \mathrm{i}\,Re\,\omega_{10}\,u_{10}, \tag{61}$$

$$\omega''_{11}(x) = s_0\omega_{10} + \mathrm{i}\,ReW_1^*\omega_{10} + ReW'_1u_{10}, \tag{62}$$

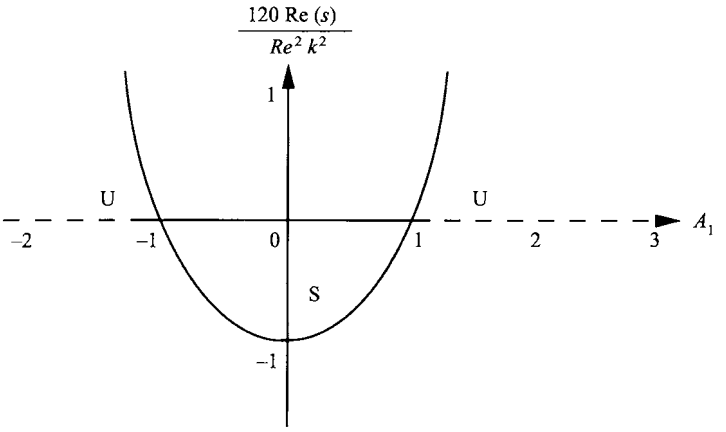

FIGURE 7. Stability criteria for the inviscid/viscous flow.

subject to the corresponding first-order boundary conditions

$$u_{11}(-1) = 0, \tag{63}$$

$$\omega_{11}(-1) = 0, \tag{64}$$

$$u_{11}(0) = 0, \tag{65}$$

$$\omega_{11}(0) = -\mathrm{i}\, u_{10}(0) - W_1'(0)\eta_1, \tag{66}$$

$$p_{11}(0) = \frac{s_0}{e}\, u_{11}(0) + \frac{s_1}{e}\, u_{10}(0) + 2\,\left[u_{11}'(0) - \mathrm{i}\, W_1'(0)\eta_1\right] + (Ca)^{-1}\eta_0, \tag{67}$$

$$Re\, u_{11}(0) = s_0\eta_1 + s_1\eta_0. \tag{68}$$

The resulting first-order eigenvalue is

$$s_1 = \left[-\tfrac{1}{4}\mathrm{i} + \tfrac{1}{120}(1 + A_1)Re\right] ReW_1'(0). \tag{69}$$

After some simplification, the temporal growth rate to the first-order can be expressed as

$$s = \tfrac{1}{4}\mathrm{i}\left[2(A_1 - 1)k + (1 - A_1)Rek^2\right] + \tfrac{1}{120}(A_1^2 - 1)Re^2k^2. \tag{70}$$

This unstable mode is similar to Lezzi & Prosperetti's (1991) $s^{(0)}$ mode. It belongs to the long-wave region and its magnitude is proportional to k^2. We plot the real part of the growth rate as a function of A_1 in figure 7. It is clear from the plot that if $W_1'(0) > 0$ or $W_1'(0) < -2$, i.e. $|A_1| > 1$, then the interface will become unstable.

For the side region of the air pocket, air is forced to flow outwards, opposite to the direction of the liquid flow. In this case, the velocity gradient at the interface (figure 5*c*) is positive, that is $W_1'(0) > 0$, thus the flow is unstable, consistent with the experimental observations. In the middle region of the air pockets, air flows in the same direction as the liquid, thus $W_1'(0)$ is negative. If $W_1'(0)$ is greater that -2, this analysis predicts a stable flow as observed in the experiments. However, when $W_1'(0) < -2$, then this asymptotic analysis predicts an unstable flow in contrast with the experimental observations. This inconsistency is due to the exclusion of shear in the liquid layer. We therefore must include the liquid layer in the analysis.

3.2. *Two viscous layers*

In this section, we extend the long-wave asymptotic analysis to consider the shear in the liquid layer. In the long-wave limit, the stream functions ($\hat{\psi}_i$), growth rate (s), and interfacial deviation ($\hat{\eta}$) can be expanded in terms of the wavenumber, k (Yih 1967)

$$\hat{\psi}_i(x,k) = \psi_{i0}(x) + k\psi_{i1}(x) + k^2\psi_{i2}(x) + \ldots, \tag{71}$$

$$s(k) = k(s_0 + ks_1 + k^2 s_2 + \ldots), \tag{72}$$

$$\hat{\eta} = -\frac{\mathrm{i}Re\psi_{i0}}{s_0^*} + \frac{\mathrm{i}s_1 Re\psi_{i0}}{s_0^{*2}}k + \ldots, \tag{73}$$

$$s_0^* = s_0 + \mathrm{i}ReW_1(0). \tag{74}$$

The zeroth-order approximation of the Orr–Sommerfeld equations is given by

$$\psi_{i0}^{\mathrm{iv}} = 0. \tag{75}$$

The boundary conditions given by

$$\psi_{10}(-1) = 0, \qquad \psi'_{10}(-1) = 0, \tag{76}$$

$$\psi_{20}(n) = 0, \qquad \psi'_{20}(n) = 0, \tag{77}$$

$$\psi_{10}(0) = \psi_{20}(0), \tag{78}$$

$$\psi'_{10}(0) - \psi'_{20}(0) = -\frac{\mathrm{i}Re\psi_{10}(0)}{s_0^*}\left(W'_2(0) - W'_1(0)\right), \tag{79}$$

$$m\psi''_{10}(0) - \psi''_{20}(0) = -\frac{\mathrm{i}Re\psi_{10}(0)}{s_0^*}\left(W''_2(0) - mW''_1(0)\right), \tag{80}$$

$$m\psi'''_{10}(0) = \psi'''_{20}(0), \tag{81}$$

are obtained by substituting (71)–(74) into (18)–(26) and collecting terms which do not contain k.

The zeroth-order solution to the above system is given by

$$\psi_{i0} = 1 + B_i\, x + C_i\, x^2 + D_i\, x^3\ , \tag{82}$$

where

$$B_1 = \frac{\mathrm{i}(A_1 - A_2)mn^2Re + (1 + 3mn^2 + 4mn^3)s_0}{2mn^2(1+n)s_0}, \tag{83}$$

$$B_2 = \frac{\mathrm{i}(A_1 - A_2)mn^3Re - (4 + 3n + mn^3)s_0}{2n(1+n)s_0}, \tag{84}$$

$$C_1 = \frac{\mathrm{i}(A_1 - A_2)mn^2Re + (1 + mn^3)s_0}{mn^2(1+n)s_0}, \tag{85}$$

$$C_2 = -\frac{\mathrm{i}(A_1 - A_2)mn^3Re + (1 + mn^3)s_0}{n^2(1+n)s_0}, \tag{86}$$

$$D_1 = \frac{\mathrm{i}(A_1 - A_2)mn^2Re + (1 - mn^2)s_0}{2mn^2(1+n)s_0}, \tag{87}$$

$$D_2 = \frac{\mathrm{i}(A_1 - A_2)mn^2Re + (1 - mn^2)s_0}{2n^2(1+n)s_0}, \tag{88}$$

$$s_0 = -\mathrm{i}mn\frac{A_1 - A_2 + (A_1 + A_2)mn^2 - 2(a_1 - a_2)(1+n)}{1 + 4mn + 6mn^2 + 4mn^3 + m^2n^4}. \tag{89}$$

Again the zeroth-order growth rate, s_0, is purely imaginary, thus it does not

provide any information regarding the stability. So the same procedure as before is followed to obtain the first-order correction. The first-order approximation to the Orr–Sommerfeld equation is given by

$$\psi_{i1}^{\mathrm{iv}} = \frac{1}{\varsigma_i}[(s_0 + \mathrm{i}ReW_i)\psi_{i0}'' - \mathrm{i}ReW_i''\psi_{i0}], \tag{90}$$

subject to the following boundary conditions:

$$\psi_{11}(-1) = 0, \quad \psi_{11}'(-1) = 0, \tag{91}$$

$$\psi_{21}(n) = 0, \quad \psi_{21}'(n) = 0, \tag{92}$$

$$\psi_{11}(0) = \psi_{21}(0), \tag{93}$$

$$\psi_{11}'(0) - \psi_{21}'(0) = -\frac{\mathrm{i}s_1 Re\psi_{10}(0)}{s_0^{*2}}\left[W_2'(0) - W_1'(0)\right], \tag{94}$$

$$m\psi_{11}''(0) - \psi_{21}''(0) = -\frac{\mathrm{i}s_1 Re\psi_{10}(0)}{s_0^{*2}}\left[W_2''(0) - mW_1''(0)\right], \tag{95}$$

$$\left[\psi_{10}'(0)s_0^* - \mathrm{i}Re\psi_{10}(0)W_1'(0)\right] - \psi_{11}'''(0) + \frac{1}{m}\psi_{21}'''(0)$$
$$-\frac{1}{e}\left(\psi_{20}'(0)s_0^* - \mathrm{i}Re\psi_{20}(0)W_2'(0)\right) = \frac{Re\psi_{10}(0)}{s_0^*}F\sin(\theta). \tag{96}$$

The solution to the first-order approximation can be written as

$$\psi_{i1} = \Delta B_i\, x + \Delta C_i\, x^2 + \Delta D_i\, x^3 + h_i(x)\mathrm{i}, \tag{97}$$

where the h_i are determined by integrating (90) four times:

$$h_1(x) = \tfrac{1}{210}\mathrm{i}A_1D_1Re\, x^7 + \tfrac{1}{60}\mathrm{i}a_1D_1Re\, x^6$$
$$+\tfrac{1}{60}(-\mathrm{i}A_1B_1Re + \mathrm{i}a_1C_1Re + 3D_1s_0)x^5 + \tfrac{1}{12}(-\mathrm{i}A_1Re + C_1s_0)x^4, \tag{98}$$

$$h_2(x) = \frac{\mathrm{i}m^2}{210e}A_2D_2Re\, x^7 + \frac{\mathrm{i}m}{60e}a_2D_2Re\, x^6$$
$$+\frac{m}{60e}(\mathrm{i}a_2C_2Re - \mathrm{i}A_2B_2mRe + 3D_2s_0)x^5 + \frac{m}{12e}(-\mathrm{i}A_2mRe + C_2s_0)x^4. \tag{99}$$

The six coefficients and the eigenvalue s_1 can be obtained by solving the boundary conditions. The first-order correction of the growth rate is in the form

$$s_1 = -\tfrac{1}{3}\mathrm{i}[s_0^2(-3mn^2(1+2n+mn^2)h_1'(1) - 3mn^2(3+4n+mn^2)h_1(1)$$
$$+3n(1+2mn+mn^2)h_2'(n) - 3(1+4mn+3mn^2)h_2(n) + \mathrm{i}a_1mn^3(1-1/e)(1+mn)Re$$
$$-B_1mn^3(1-1/e)(1+mn)s_0) - Fmn^3(1+mn)Res_0\sin(\theta)]/mn^2Re(2(a_1-a_2)(1+n)$$
$$-(A_1-A_2)(1-mn^2)). \tag{100}$$

This long-wave asymptotic result (100) is the most general solution for the two-layer parallel flow. Unlike previous cases studied (Yih 1967; Yiantsios & Higgins 1988; Hooper 1989; etc.), here A_1 does not equal A_2 because we have taken the density difference and inclination angle into consideration. Also we have an extra term $[W_2''(0) - mW_1'']\eta$ in the tangential continuity condition (22). These two unique terms in our calculation make the result more general and applicable to our air entrainment experiments (Aidun *et al.* 1992). The expression for the growth rate presented by (100) reduces to Yih's (1967) expressions for the two-layer Poiseuille flow by allowing the inclination angle θ to be 90° while limiting the two layers to equal density and

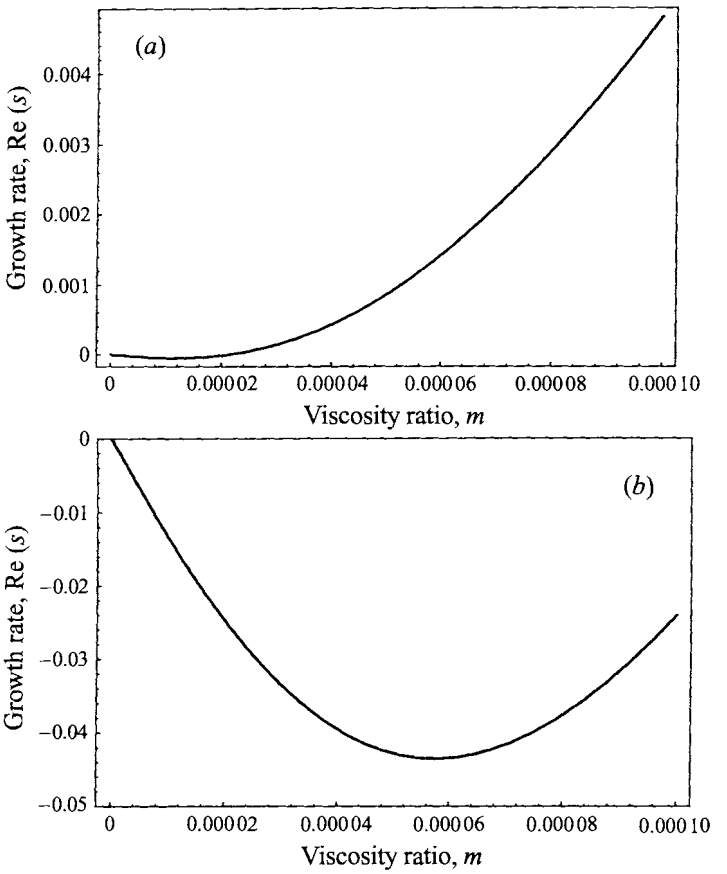

FIGURE 8. Stability of (*a*) the side region of the triangular air layer (B-B) and (*b*) the middle region of the triangular air layer (A-A) for various viscosity ratios.

thickness with stationary walls. Equation (100) can also be reduced to Yih's (1967) expressions for Couette flow (i.e. $r = 1, A_1 = A_2 = 0$).

We now apply the result to our air entrainment experiments where the density ratio of air to liquid is taken as $e = 0.001207$. The inclination is considered to be vertical, that is $\theta = 0°$ and the thickness ratio $n = 10$.

As stated before, we break down and approximate the flow near the sides of the air pocket with a parallel counter-current Couette–Poiseuille system where the net flow of air is in the opposite direction to the liquid flow. Figure 8(*a*) shows the variation in growth rate with the viscosity ratio. The experiments cover the range $2.57 \times 10^{-5} \leqslant m \leqslant 1.20 \times 10^{-4}$. For all m, the interface for this flow is unstable as observed in the experiments.

The interfacial stability of the middle section of the air pocket is studied by allowing air and liquid to move in the same direction. For the viscosity ratio m in the experimental region, the middle section is stable as shown in figure 8(*b*) which is also consistent with the experiments. Though asymptotic analysis gives us results in the long wave-limit consistent with the experimental observations, we still want to find out whether the results in other wave region would also agree with experiments. In the following section, we show the numerical results of the stability analysis in the whole wave range.

4. Stability analysis: method

As explained in the previous section, the long-wave approximation is not sufficient to explain the stability characteristics of the air/liquid interface in our air entrainment experiments. The interface could be unstable to an interfacial mode with a finite wavenumber or unstable to a completely different mode. From previous studies of two-layer Poiseuille flows (Yiantsios & Higgins 1988), we know that the shear mode is a candidate. But, are there other modes that may become unstable in this system that have not been captured in previous studies? By computational analysis and parametric continuation of the solution to the Orr–Sommerfeld equation for the two-layer Poiseuille–Couette flow in inclined channels, we obtain all of the possible modes that could become unstable in this system.

The numerical scheme chosen for this system is the Chebyshev-Tau method (Gottlieb & Orszag 1977). The Tau method is preferred because it automatically satisfies all boundary conditions. Since the Chebyshev polynomials span the range between -1 and 1, we transfer the coordinate x to x_t for each layer where x_t is given by

$$x_t = \begin{cases} 2\left(x+\frac{1}{2}\right), & -1 \leqslant x \leqslant 0 \\ (2/n)\left(x-\frac{1}{2}n\right), & 0 < x \leqslant n. \end{cases} \tag{101}$$

The stream function for each layer, $\psi_i(x)$, is expanded in a truncated Chebyshev polynomial series

$$\psi_i(x) = \sum_{j=0}^{N_i} a_{i,j} T_j(x_t), \tag{102}$$

where the subscript i equals 1 or 2 depending on the layer and $T_j(x)$ are Chebyshev polynomials (Gottlieb & Orszag 1977) defined as

$$T_j(\cos\beta) = \cos(j\beta). \tag{103}$$

The truncation numbers (N_i) are selected to be large enough for sufficient accuracy. The total number of unknowns is $(N_1 + N_2 + 3)$. A total of $(N_1 - 3)$ equations for layer 1 and $(N_2 - 3)$ for layer 2 are constructed by taking advantage of the orthogonal property of the Chebyshev polynomials. Together with the nine boundary conditions, a generalized eigenvalue problem can be defined:

$$\begin{pmatrix} h_{11} & h_{12} & h_{13} \\ h_{21} & h_{22} & h_{23} \\ h_{31} & h_{32} & h_{33} \end{pmatrix} \begin{pmatrix} a_{1,j} \\ a_{2,j} \\ \eta \end{pmatrix} = s \begin{pmatrix} b_{11} & b_{12} & b_{13} \\ b_{21} & b_{22} & b_{23} \\ b_{31} & b_{32} & b_{33} \end{pmatrix} \begin{pmatrix} a_{1,j} \\ a_{2,j} \\ \eta \end{pmatrix}. \tag{104}$$

The transformation of the base states (8) and (9), Orr–Sommerfeld (16), and the boundary conditions will not be discussed in this paper, and can be found elsewhere (Severtson 1996). The coefficients in these linear equations depend on the parameters in the problem including the wavenumber k. It should be noted that by transforming the original equations into the above algebraic equations all possible growth rates now appear as the eigenvalues in this system, and an eigenvalue with a positive real part indicates an unstable mode.

The neutral stability curve can be traced by continuation of the solution from the long-wave approximation or from the generalized eigenvalue problem as the initial point of continuation. Our strategy is to treat the system of first-order differential equations as a dynamical system. The neutral stability curve can then be obtained through the use of a pseudoarclength continuation method by forcing

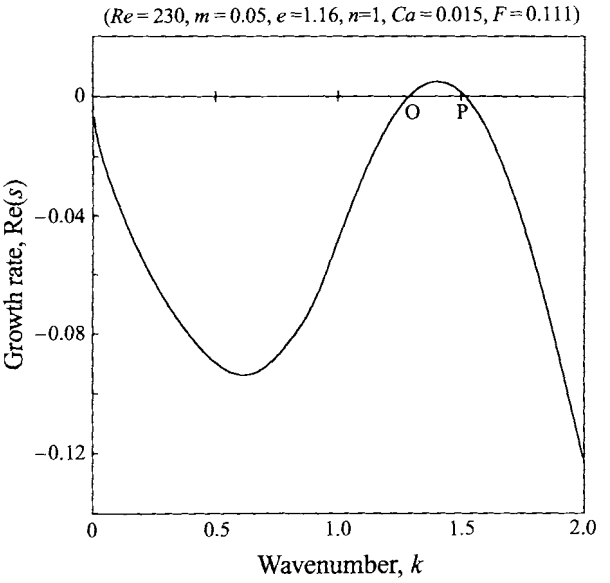

FIGURE 9. Reproduction of the unstable shear mode for Yiantsios & Higgins' Poiseuille flow (1988).

the real part of the growth rate to be zero. The continuation is done with AUTO, software developed by Doedel & Kerneves (1986). To verify the numerical solution, we reproduce Renardy's (1985) two-layer Couette flow case as well as interfacial and shear (figure 9) modes for the two-layer Poiseuille flow problems reported by Yiantsios & Higgins (1988).

5. Stability analysis: results and discussions

In order to obtain the stability characteristics of the air entrainment problem, we have to analyse the stability modes of Poiseuille–Couette flow in an inclined channel. We first obtain the unstable modes of this flow in a horizontal channel. Then, we apply the results to the air/liquid system.

5.1. *Poiseuille–Couette flow with horizontal walls*

In the horizontal case where the inclination angle $\theta = 90°$, Couette flow occurs in both layers when

$$\frac{\mathrm{d}p}{\mathrm{d}z} - \rho_1 g \cos(\theta) = 0, \tag{105}$$

$$\frac{\mathrm{d}p}{\mathrm{d}z} - \rho_2 g \cos(\theta) = 0. \tag{106}$$

The two possible situations for the above conditions to be realized are if $\theta = 90°$ with zero pressure gradient or if both layers have equal density and the pressure gradient equals $\rho_1 g \cos(\theta)$. In this section we consider the first case, i.e. a horizontal Poiseuille–Couette flow ($\theta = 90°$). To investigate the stability characteristics of this system in terms of the transition from a Poiseuille to a Couette system, we define the left-wall velocity coefficient (r) as the homotopy parameter. Starting with pure Poiseuille flow, that is $r = 0$, we gradually impose a Couette component by increasing

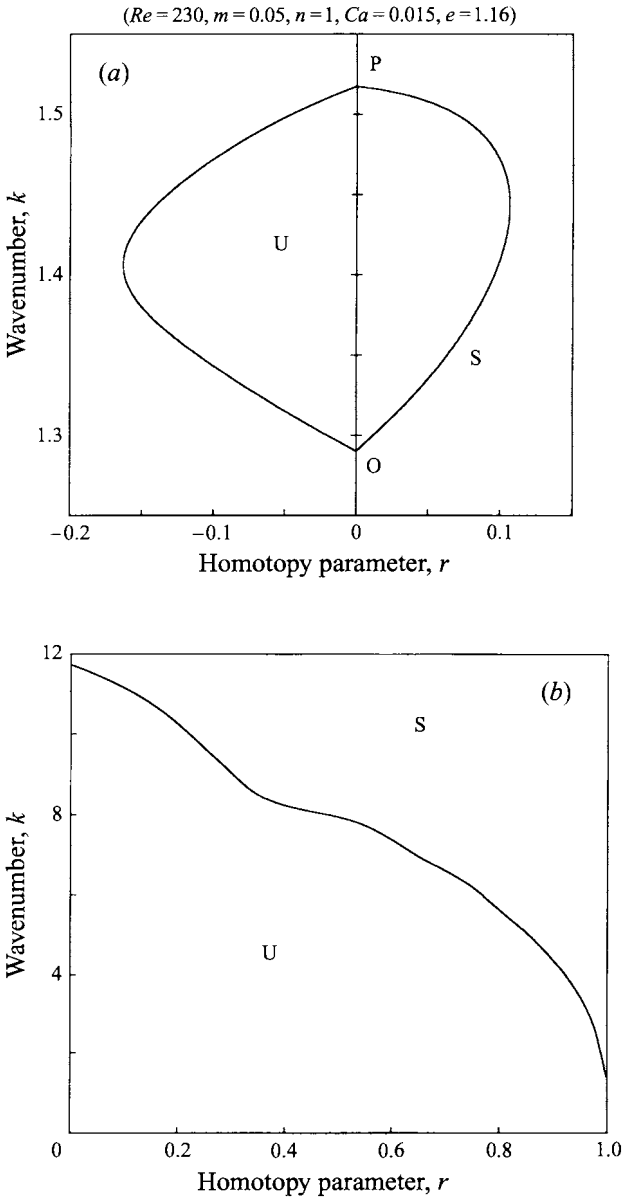

FIGURE 10. Effect of the Couette component on the stability of (*a*) the shear mode and (*b*) the interfacial mode.

r. Meanwhile we decrease the pressure gradient ($\mathrm{d}p/\mathrm{d}z$) according to the relation:

$$\frac{\mathrm{d}p}{\mathrm{d}z} = \begin{cases} (1-r)\mathrm{D}P/\mathrm{D}Z, & r \geqslant 0, \\ (1+r)\mathrm{D}P/\mathrm{D}Z, & r < 0, \end{cases} \tag{107}$$

where $\mathrm{D}P/\mathrm{D}Z$ denotes the corresponding pressure gradient of the pure Poiseuille system. When $|r|$ becomes 1, the system becomes a purely Couette flow. A positive value of r means the left wall is moving in the direction of positive z-axis, while a negative value means it is moving in the opposite direction.

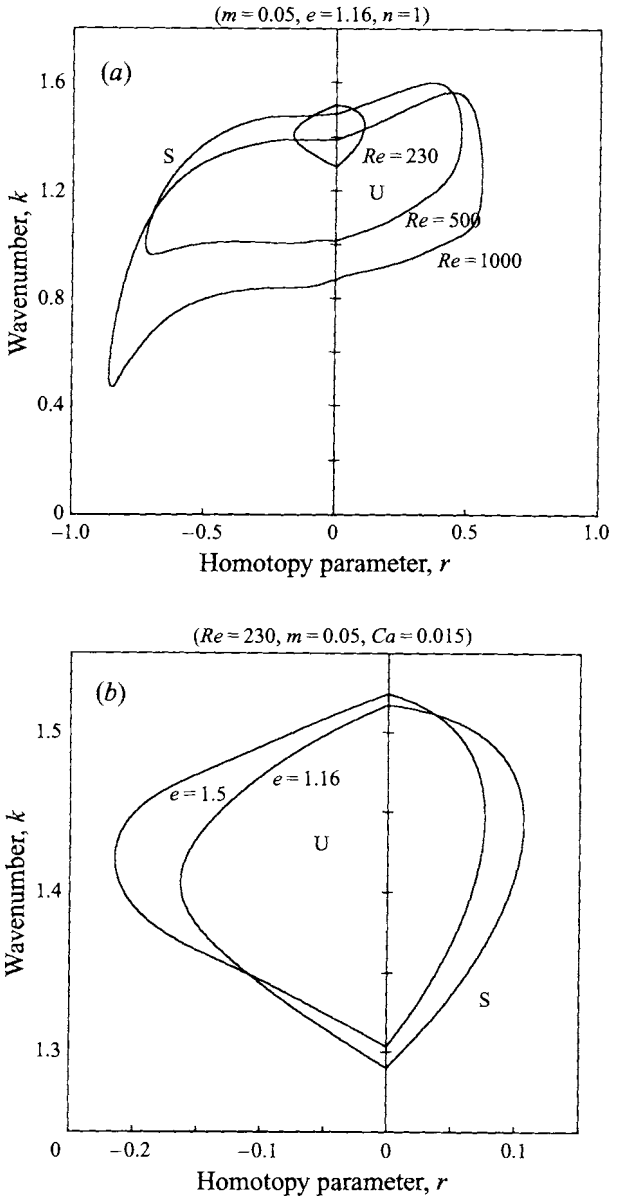

FIGURE 11(*a*, *b*). For caption see facing page.

In defining the Poiseuille–Couette system this way, we keep the Reynolds number the same throughout the transition. The Reynolds number is defined as the sum of the Couette and Poiseuille components, that is

$$Re = Re_c + Re_p, \tag{108}$$

where each component is defined by

$$Re_c = |r|\ Re, \quad Re_p = (1 - |r|)\ Re. \tag{109}$$

Figure 10(*a*) is the resulting neutral stability curve for the shear mode at Reynolds number 230. Points O and P in the figure where the neutral stability curve intersects

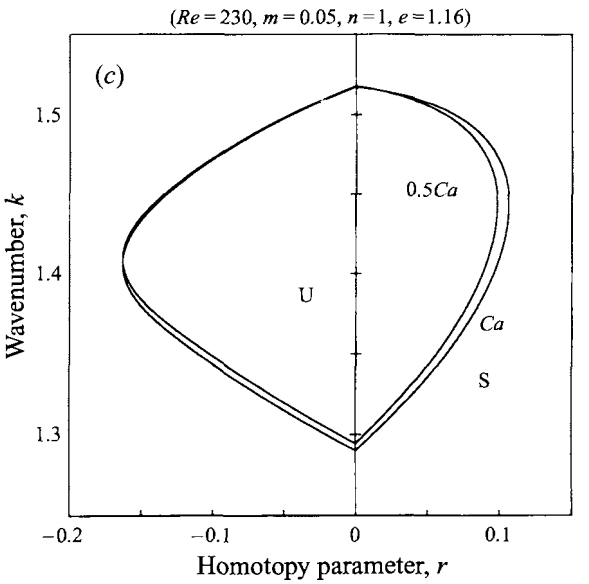

FIGURE 11. Effect of (*a*) Reynolds number (*b*) density ratio and (*c*) capillary number on the efficiency of the Couette component.

with the $r = 0$ axis correspond to the points O and P of the Yiantsios and Higgins' case in figure 9. The continuation of these points for $|r| > 0$ shows that the Couette component stabilizes the shear mode. After superposing enough Couette component into the system, the shear mode is totally stabilized. When the left wall is moving opposite to the positive z-axis, more Couette component is required to completely stabilize the shear mode.

Similar to the shear mode, the interfacial mode (figure 10*b*) at the same Reynolds number (230) is also stabilized also by addition of the Couette component. But there is a significant difference – the interfacial mode is never totally stabilized, even for a pure Couette flow.

As the Reynolds number increases, the unstable shear mode region increases (figure 11*a*) and more Couette component is required for complete stability.

The effect of the density stratification on stability varies based on the direction of the moving wall (figure 11*b*). If the wall is moving in the same direction as the pressure gradient, the increasing density ratio destabilizes the shear mode. On the other hand, if the wall is moving opposite to the pressure gradient, then the increasing density ratio will stabilize the shear mode. The effect of capillary number on the shear mode of instability is insignificant as one expects (figure 11*c*).

5.2. *Application to air/liquid flow*

Finally we apply the stability analysis to the air/liquid experiments. Figure 12(*a*) is the most dangerous mode for the middle region of the air pocket with the base-state velocity profile shown in figure 5(*b*). The real part of the growth rate is always negative indicating that the flow is always stable in this region. On the other hand, the most dangerous mode for the side region of the air pocket, with velocity profile shown in figure 5(*c*), has positive growth rate as shown in figure 12*b*. The flow at the side region is unstable to the interfacial mode, only.

These results are consistent with the experimental observations. Moreover, the

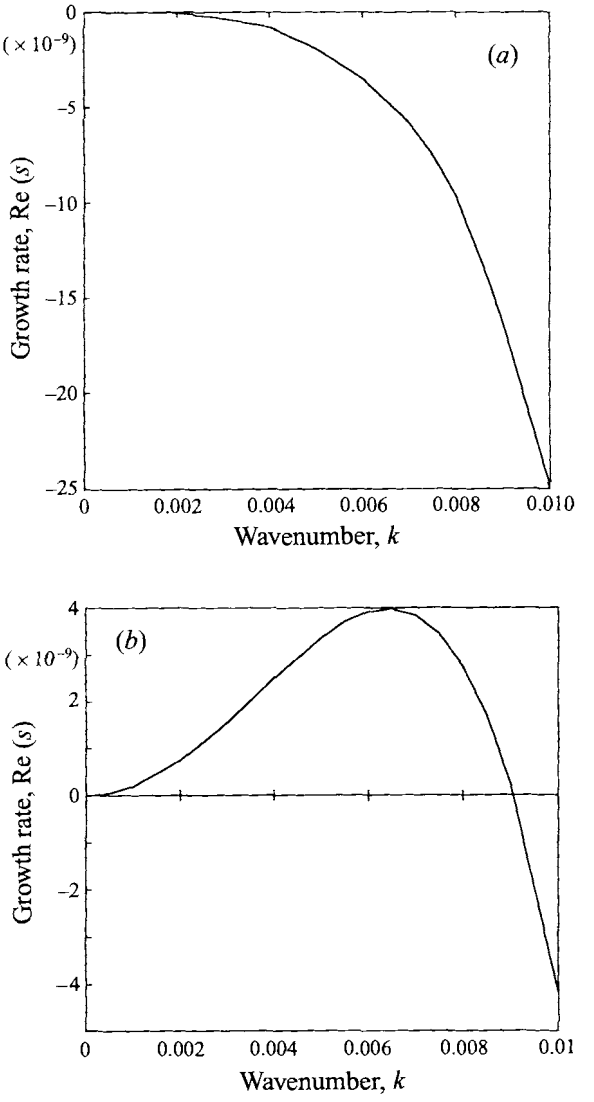

FIGURE 12. The most dangerous mode for the air/liquid experiment; (*a*) the middle region, (*b*) the side region.

interfacial mode for the side region of the air pocket is unstable at wavenumbers of the order of 10^{-3}, which agrees with the scale of the wavelength recorded in the experiments.

6. Conclusions

Our flow visualization studies (Aidun *et al.* 1992) reveal a sequence of events leading to the formation and entrainment of air bubbles into the liquid phase. This mode results in the formation of visible air bubbles and is referred to as 'excessive' air entrainment. The air bubbles can remain adjacent to the solid surface, as shown in curtain coating experiments (Kistler 1984), or get entrained into the liquid stream,

as demonstrated in our experiments. The mechanism of air bubble formation and its entrainment into the liquid phase has been investigated in this study.

The long-wave stability analysis is applied to inviscid/viscous and viscous/viscous layers. Both results indicate that the only unstable mode is an interfacial mode with growth rate starting at $k = 0$ proportional to k^2. This mode of instability is similar to one of the long-wave modes for flow down an inclined plane studied by Benjamin (1957) and Yih (1963). It is interesting to note that the long-wave approximation for this problem does not admit the Kelvin–Helmholtz modes reported by Lezzi & Prosperetti (1991) for their air entrainment system. Long-wave analysis shows that the flow at the side of the air pocket is unstable and the flow in the middle region of the air pocket is stable, which is consistent with the experimental results.

The Chebyshev-Tau method is used to obtain the full spectrum of critical modes possible in the two-layer Poiseuille–Couette flow in inclined channels. The interfacial mode is the dominant mode of instability although the shear mode is always present if the Couette component is not too large.

Full stability analysis of the air/liquid flow in the experiments show that flow in the mid region is always stable while the side regions are always unstable. This is consistent with experimental observations. The only critical mode we have found for the base state which corresponds to our experiments is the interfacial mode with wavenumber of about 10^{-3}. This wavelength compares well with the experimental approximations.

We have also found a new mode of instability when there is an interfacial inflection point in the base velocity. The mode, which is analogous to the inviscid mode in boundary layer flows, has been fully explored and results will be published in the near future (Aidun & Severtson 1996).

The authors would like to thank Dr Marc Smith for helpful discussions. This study has been supported by the National Science Foundation through grant CTS-9258667, and by industrial matching contributions. The calculations were conducted, in part, using the National Center for Supercomputing Applications, a resource at Cornell University which is funded by the National Science Foundation, IBM, and New York State.

REFERENCES

AIDUN, C. K. & SEVERTSON, Y. C. 1996 A new mode in two-layer stratified flow in inclined channels. In preparation.

AIDUN, C. K., VEVERKA, P. J. & SCRIVEN, L. E. 1991 Onset of air entrainment: Mechanism. *AIChE Annual Meeting*, Paper No.11b.

AIDUN, C. K., VEVERKA, P. J. & SCRIVEN, L. E. 1992 Interfacial instability and excessive air entrainment. *AIChE Spring National Meeting*, Paper No.49A.

BENJAMIN, T. B. 1957 Wave formation in laminar flow down an inclined plane. *J. Fluid Mech.* **2**, 554.

BLAKE, T. D. & RUSCHAK, K. J. 1979 A maximum speed of wetting. *Nature* **282**, 489.

DERYAGIN, B. M. & LEVI, S. M. 1959 *Film Coating Theory*. Focal Press, London.

DOEDEL, E. & KERNEVES, J. P. 1986 Auto: Software for continuation and bifurcation problems in ordinary differential equations.

GOTTLIEB, D. ORSZAG, S. A. 1977 *Numerical Analysis of Spectral Methods*. SIAM.

HOOPER, A. P. 1989 The stability of two superposed viscous fluids in a channel. *Phys. Fluids* A **1**, 1133.

HOOPER, A. P. & BOYD, W. G. C. 1983 Shear-flow instability at the interface between two viscous fluids. *J. Fluid Mech.* **128**, 507.

HOOPER, A. P. & BOYD, W. G. C. 1987 Shear-Flow instability due to a wall and a viscosity discontinuity at the interface. *J. Fluid Mech.* **179**, 201.

KISTLER, S. F. 1984 The fluid mechanics of curtain coating and related viscous free surface flows with contact lines. PhD Dissertation, University of Minnesota.

LEZZI, A. M. & PROSPERETTI, A. 1991 The stability of an air film in a liquid flow. *J. Fluid Mech.* **226**, 319.

LOEWENHERZ, D. S. & LAWRENCE, C. J. 1989 The effect of viscosity stratification on the stability of a free surface flow at low Reynolds number. *Phys. Fluids* A **1**, 1686.

MIYAMOTO, K. 1991 On the mechanism of air entrainment. *Indust. Coating Res.* **1**, 71.

MIYAMOTO, K. & SCRIVEN, L. E. 1982 Breakdown of air film entrained by liquid coated on web. *AIChE Annual Meeting, Los Angeles, CA.*

RENARDY, Y. Y. 1985 Instability at the interface between two shearing fluids in a channel. *Phys. Fluids* **28**, 3341.

RENARDY, Y. Y. 1987 The thin-layer effect and interfacial stability in a two-layer Couette flow with similar liquids. *Phys. Fluids* **30**, 1627.

REYNOLDS, W. C. & POTTER, M. C. 1967 Finite-amplitude instability of parallel shear flows. *J. Fluid Mech.* **27**, 465.

SCRIVEN, L. E. 1982 How does air entrain at wetting lines. *AIChE Spring National Meeting, Orlando, FL.*

SEVERTSON, Y. C. 1996 Stability analysis of thin film coating systems. PhD Dissertation, Georgia Institute of Technology.

SMITH, M. K. 1990 The mechanism for the long-wave instability in thin liquid films. *J. Fluid Mech.* **217**, 469.

TILLEY, B. S., DAVIS, S. H. & BANKOFF, S. G. 1994 Linear stability theory of two-layer fluid flow in an inclined channel. *Phys. Fluids* **6**, 3906.

VEVERKA, P. J. & AIDUN, C. K. 1991 Air entrainment and dynamic contact line instability in low speed roll coating. *Tappi J.* **74**(9), 203.

YIANTSIOS, S. G. & HIGGINS, B. G. 1988 Linear stability of plane Poiseuille flow of two superposed fluids. *Phys. Fluids* **31**, 3225.

YIH, C. S. 1963 Stability of liquid flow down an inclined plane. *J. Fluid Mech.* **6**, 321.

YIH, C. S. 1967 Instability due to viscosity stratification. *J. Fluid Mech.* **27**, 337.